AIAA JOURNAL
Vol. 57, No. 7, July 2019

Check for updates

Effect of Coherent Structures on Aero-Optic Distortion in a Turbulent Boundary Layer

Theresa Saxton-Fox* and Beverley J. McKeon†
California Institute of Technology, Pasadena, California 91125
and
Stanislav Gordeyev‡
University of Notre Dame, Notre Dame, Indiana 46556

DOI: 10.2514/1.J058088

The deflection of a small-aperture laser beam was studied as it passed through an incompressible turbulent boundary layer that was heated at the wall. The heating at the wall was sufficiently mild that the temperature and density fields acted as passive scalars with a Prandtl number of 0.71. Simultaneous particle image velocimetry and Malley probe laser deflection measurements were performed in overlapping regions of the boundary layer to identify correlations between coherent velocity structures, passive scalar transport, and optical beam deflection. Streamwise gradients in the streamwise and wall-normal velocity fields were observed to be correlated to the deflection of the optical beam and to streamwise density gradients. The passage of a large-scale motion through the beam path was shown to affect the statistics of the optical beam deflection as well as the local distribution of small-scale velocity features. The wall-normal small-scale velocity features were consistently correlated to the beam deflection, throughout different phases of the large-scale motion convection. The observations motivated a hypothesis that views the large scales as heat carriers, whereas the small scales modify the local sense of a velocity and density gradient toward a streamwise gradient that directly affects the optical beam deflection.

Downloaded by UNIVERSITY OF NOTRE DAME on July 5, 2019 | http://arc.aiaa.org | DOI: 10.2514/1.J058088

Nomenclature

C_p	=	specific heat capacity of air
K_{GD}	=	Gladstone–Dale constant
k_x, k_z	=	streamwise and spanwise wave numbers
n	=	index of refraction
p_x	=	optical momentum
q_w	=	wall heat flux
R	=	projection coefficient
Re_Θ	=	Reynolds number defined using the momentum thickness $U_\infty\Theta/\nu$
Re_τ	=	Reynolds number defined using the friction velocity $u_\tau\delta/\nu$
S	=	wave front
T_{hw}	=	temperature of the heated wall
T_τ	=	friction temperature
T^*	=	dimensionless temperature
U, V	=	streamwise and wall-normal velocity fields
U_∞	=	freestream velocity
u, v	=	fluctuating streamwise and wall-normal velocity fields
u_s, v_s	=	small-scale streamwise and wall-normal velocity fields
u_τ	=	friction velocity
$\tilde{u}$	=	velocity model
$\hat{u}$	=	wall-normal coherence of velocity model
x, y, z	=	streamwise, wall-normal, and spanwise coordinates
x_T	=	streamwise distance from a step change in thermal boundary condition
x^γ	=	phase shifted streamwise coordinate
$\hat{x}$	=	streamwise coordinate centered at Malley probe location
γ	=	phase
δ	=	99% boundary-layer thickness
δ_T	=	thermal boundary-layer thickness
ζ	=	parameterization variable along optical beam path
Θ	=	momentum thickness
θ	=	streamwise deflection angle of Malley probe (– upstream, + downstream)
Λ	=	field of view of the data
λ_G	=	Gaussian filter approximate cutoff wavelength
ρ	=	density
ρ_a	=	ambient density
σ	=	standard deviation
σ_G	=	Gaussian filter standard deviation
$\langle\rangle$	=	averaged quantity

I. Introduction

When a laser beam passes through changes in the index of refraction in a turbulent flow, the beam path and wave front become distorted in time [1–3]. Such changes in the index of refraction can occur from the mixing of two fluids of different indices [4], from density variation in compressible flows [5], and from density variation in heated flows [6], to name a few. One can use active optics to mitigate the distortion of the optical beam in these systems; this has been done for astronomical telescopes to correct for the density variation in the atmosphere [7]. However, for many turbulent flows, the frequencies present are much higher than those in the atmospheric boundary layer, making the implementation of active correction techniques much more challenging [4]. Improved understanding of the flow features that are responsible for the distortion has been sought in order to advance control methodologies. Identifying these flow features is made challenging by the integral nature of the aero-optic system: the laser beam passes through the whole flowfield, potentially being affected by multiple events or scales along its trajectory before exiting the variable-density region.

Previous work on the aero-optic problem in compressible turbulent boundary layers identified a characteristic convection velocity of the distortions by correlating the signals of two streamwise-adjacent beams [5]. The identified convection velocity of $0.82U_\infty$, where U_∞ was the freestream velocity, suggested a correlation between optical distortion and flow events in the outer region of the boundary layer. In the outer region of the boundary layer, large-scale motions are

Received 8 November 2018; revision received 3 February 2019; accepted for publication 5 February 2019; published online 12 April 2019. Copyright © 2019 by the American Institute of Aeronautics and Astronautics, Inc. All rights reserved. All requests for copying and permission to reprint should be submitted to CCC at www.copyright.com; employ the eISSN 1533-385X to initiate your request. See also AIAA Rights and Permissions www.aiaa.org/randp.

*Assistant Professor, Department of Aerospace Engineering, University of Illinois at Urbana–Champaign, 104 S Wright St., Urbana, IL 61801.

†Theodore von Karman Professor of Aeronautics, Graduate Aerospace Laboratories, MC 105-50. Associate Fellow AIAA.

‡Associate Professor, Department of Aerospace and Mechanical Engineering, 121 Hessert Laboratory. Associate Fellow AIAA.

Downloaded by UNIVERSITY OF NOTRE DAME on July 5, 2019 | http://arc.aiaa.org | DOI: 10.2514/1.J058088

the dominant energetic structures, with a characteristic streamwise length scale of 2–5δ [8]. In addition, smaller scales associated with hairpin vortices have been reported by many researchers [9–11]. The large-scale motions and hairpin vortices dominate the velocity and vorticity fields of the outer region of the boundary layer, but it is the index of refraction field that affects the optical system. Thus, knowledge of the effect of these well-known velocity and vorticity features on the transport of the index of refraction field, which is a scalar field, is needed.

One way to explore the relevance of velocity coherent structures on the distortion of optical beams is to estimate the density field based upon the velocity field. One such approach used the strong Reynolds analogy instantaneously to predict the scalar field from the velocity field for compressible, subsonic boundary layers [5]. Gordeyev et al. [5] showed that measured wave fronts and predicted wave fronts were in agreement most of the time. Another approach used a resolvent analysis of the Navier–Stokes and passive scalar equations to estimate scalar modes associated with given velocity modes [12]. Estimating the scalar field from the velocity field is made complicated by the fact that the relationship between the scalar and velocity fields in turbulent flows is a topic of ongoing research, even for passive scalar, unity Prandtl number flows. Statistically, differences between the scalar and streamwise velocity fields were observed in the tails of the probability density function (exponential in the scalar field rather than Gaussian [13]) and in the small-scale anisotropy of the scalar field [14]. Instantaneously, the gradients of the scalar field were also observed to be sharper than those in the velocity field, known as the "unmixedness of the scalar" [15], and features of the velocity and scalar fields were visibly not equivalent in direct numerical simulation of heated turbulent channel flows [16]. At times, greater similarity was observed instantaneously between the sum of the squared velocity fields ($u^2 + v^2 + w^2$) and the fluctuating scalar field than between the streamwise velocity and scalar fields [16]. In this work, no assumptions were used regarding the relationship between the velocity and scalar fields, and thus the density field was not quantitatively estimated from the velocity field. Instead, conditional averaging was used to connect the measured optical distortion to the measured velocity field; and conceptual, qualitative models for the density field were deduced from these connections.

In previous studies, conditionally averaging based upon the optical distortion showed that, during wave front distortion events, specific velocity events consistently occurred [17]. During positive wave front distortions, Q2 velocity events were observed near the wall. In addition, the Reynolds stresses were observed to be stronger near the wall and weaker away from it. In conditioning on negative wave front distortions, sweep-type Q4 events were observed near the middle of the boundary layer. Significantly larger Reynolds stresses were observed throughout the boundary layer than what was observed during positive wave front distortions. Vanderwel and Tavoularis [18] showed that specific coherent structures in the velocity and vorticity fields had a significant effect on the mixing of a scalar. In particular, uniform momentum zones in the streamwise velocity field were associated with but not equivalent to uniform concentration zones in the scalar field, and hairpin vortices were correlated to significant scalar fluxes.

In this study, the source of the index of refraction change was heat. The experiment was carried out in an incompressible wind tunnel with a heated wall, over which a turbulent boundary layer was developed. Within the turbulent boundary layer, the heating created a thermal boundary layer [19], within which temperature variations (and therefore density variations) were present. Gordeyev et al. [6] previously demonstrated that heating the wall of a compressible turbulent boundary layer amplified the aero-optic signal of a beam passing through the flow. The present experiment exclusively used heating at the wall to generate index of refraction change. The heating was sufficiently minimal that it was passive in the flow. This heated, incompressible flow setup led to an optical beam deflection spectrum that was similar to the spectra observed for compressible turbulent boundary layers when the frequencies were scaled using the freestream velocity and the boundary-layer thickness [20]. In addition, the convection velocity identified by correlating the deflection signals of streamwise-adjacent optical beams in the heated, incompressible flow was observed to be similar to that in the compressible flow, at $0.83U_\infty$.

In Sec. II, the experimental setup to create the thermal boundary layer and perform velocity and aero-optic measurements is discussed. In Sec. III, two models are discussed. The first is a model for the relationship between the aero-optic measurement and the scalar field, which is used for conceptual understanding of the aero-optic measurement. The second is a simple model for the large-scale motions in the streamwise velocity field, which is used for some of the analysis methods that are discussed in Sec. IV. In Sec. V, the conditional statistics of the velocity and aero-optic data are shown and described. In Sec. VI, these results are discussed and hypotheses for the relationship between coherent structures and scalar mixing are explored. Finally, in Sec. VII, the results and hypotheses are summarized and directions of potential future work are mentioned.

II. Experimental Methods

Simultaneous velocity and aero-optic measurements were conducted in the Merrill wind tunnel at the California Institute of Technology; it is an incompressible, recirculating wind tunnel. The boundary layer was tripped into a turbulent state at the leading edge of a flat plate and was allowed to develop in a nominally zero-pressure-gradient environment. Two sections of the flat plate were heated throughout their span using embedded rubber resistance heaters. Each heated section was 0.63 m long, and there was a 0.14 m unheated section between them for experimental convenience, shown schematically in Fig. 1a. A thermal camera (FLIR A325sc no. 48001-1001) was used to examine the spatial variation of the temperature across the plate, which was found to vary by about 3°C, with the warmest region at the center and the coolest regions near the edges of the plate. The resolution of the thermal camera was ±0.8°C.

The temperature of the plate was held constant at 22°C above the freestream temperature such that the flow was moderately heated. The Prandtl number of the flow was 0.71, assuming a temperature of 25°C, and using $Pr = \mu c_p/k$ with standard values for air at atmospheric pressure. This Prandtl number indicated a slightly larger diffusion of heat than of momentum in the boundary layer. The mean and variance velocity profiles were examined with and without heat addition. No change was observed in the two conditions, indicating that the heat addition acted as a passive scalar that did not affect the behavior of the velocity field. Cold-wire measurements were carried out at two locations, marked H (heated) and U (unheated) in Fig. 1a. The mean and variance temperature profiles are shown in Fig. 2 from cold-wire measurements performed by Rought [21].

Measurements are shown in Fig. 2 at three Reynolds numbers: $Re_\theta = 1700$, 2180, and 2720. Solid symbols indicate measurements taken at measurement location U, whereas empty symbols indicate measurements taken at location H. The normalized temperature is plotted, defined as $T^* = (T_{hw} - T)/T_\tau$ where T_{hw} is the temperature of the heated wall and $T_\tau = q_w/(\rho C_p u_\tau)$. q_w is the wall heat flux, ρ_a is the ambient density of air, C_p is the specific heat capacity of air, and u_τ is the friction velocity. The mean temperature profiles are compared to data from Antonia et al. [19], shown in teal stars at $Re_\theta = 3070$. Agreement is seen between the cold-wire data measured directly over the heated plate (measurement location H) and the canonical thermal boundary layer from Antonia et al. [19]. The data that were measured downstream of the end of the heated plate (measurement location U) deviated from a canonical thermal boundary layer at a height of $y^+ = 100$ or $y/\delta = 0.1$. The deviation appears as an approximately constant mean temperature condition in Fig. 2a and as a decrease in the root mean square of the temperature signal in Fig. 2b.

Heating portions of the wall led to the development of internal thermal layers, and therefore targeted heating in the boundary layer. Previous work in compressible boundary layers indicated that the convection velocity of aero-optic distortions was approximately $0.82U_\infty$ [5], putting the average height of potentially relevant structures at about 0.6δ using Taylor's hypothesis and the present work's mean velocity field. This observation motivated a study of the relationship between structures in the outer boundary layer and

Downloaded by UNIVERSITY OF NOTRE DAME on July 5, 2019 | http://arc.aiaa.org | DOI: 10.2514/1.J058088

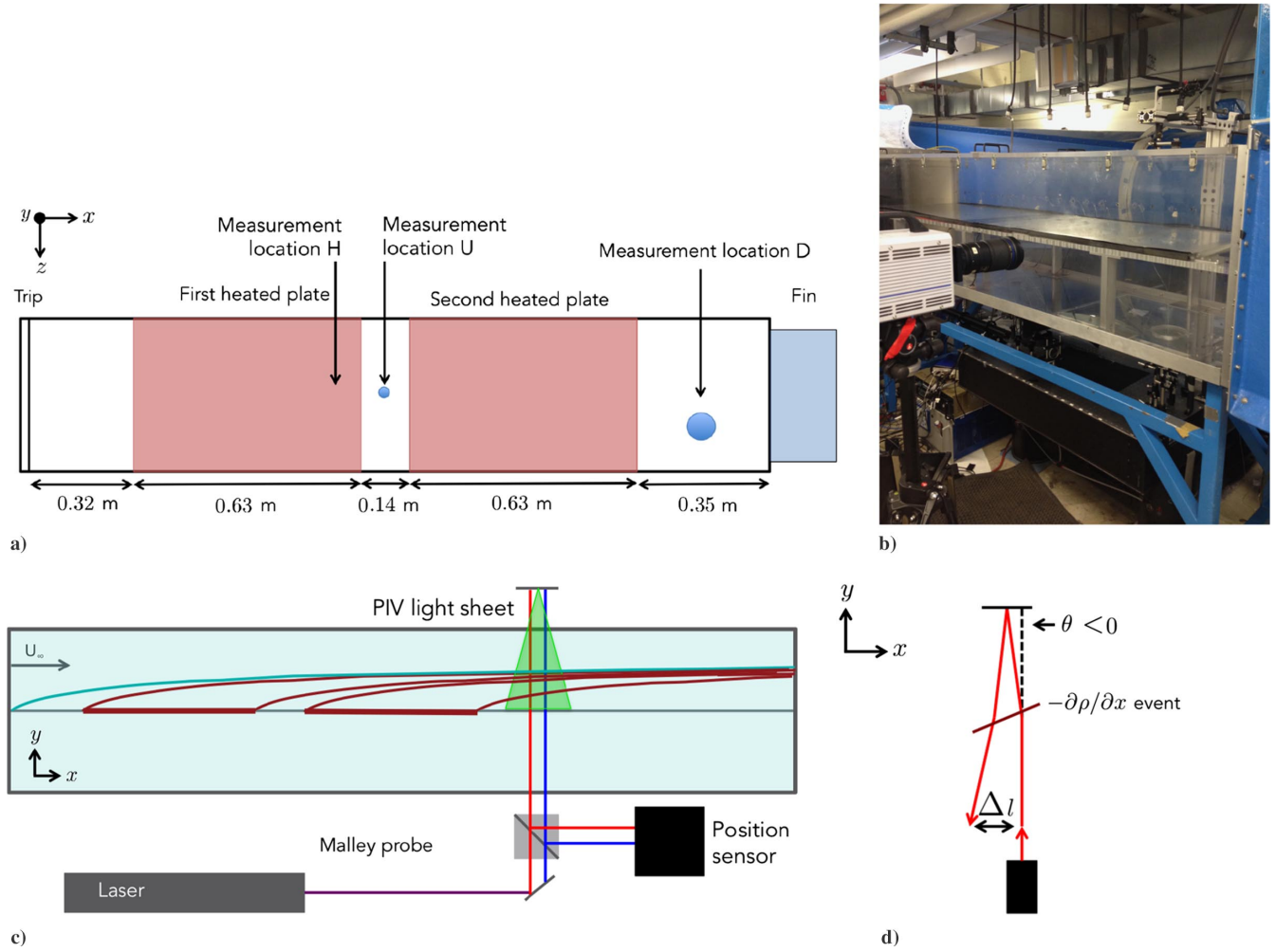

Fig. 1 Experimental setup: a) bird's eye, b) side image, c), side schematic, and d) laser bending schematic.

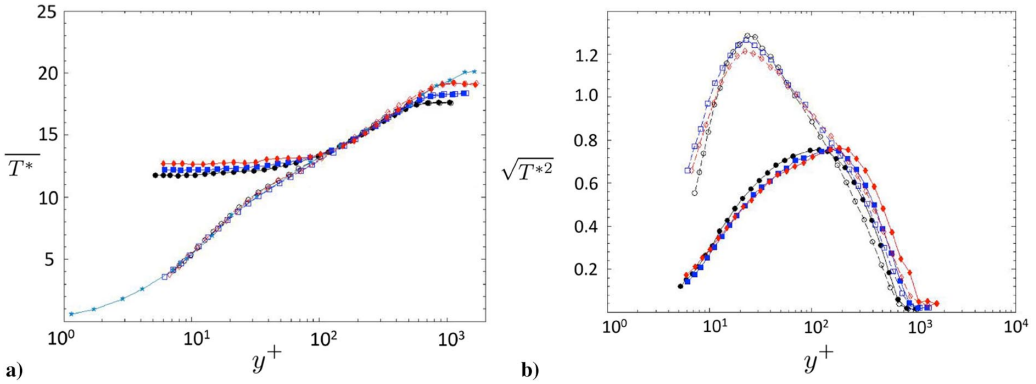

Fig. 2 Temperature statistics: a) mean with comparison to Antonia et al. [19], and b) root mean square.

aero-optic distortion. The heating at the wall, shown in Fig. 1a, led to a mean temperature profile at measurement location D that matched that of a canonical thermal boundary layer when y/δ was greater than 0.15 and less than 0.85. Outside of this region, the mean temperature profile showed less variation with height than would be present in a canonical thermal boundary layer. This heating condition effectively targeted the region y/δ near 0.6 in the flow, highlighting the structures of most interest. Data from this heating geometry compared favorably to data taken in compressible facilities both with and without heating, suggesting that the targeted heating condition reflected a focus on the appropriate region of the boundary layer, confirming the hypothesis that these structures were primarily responsible for aero-optic distortion [20]. The estimation of the mean temperature profile at the measurement location was evaluated using a combination of the cold-wire measurements shown in Fig. 2 and extrapolation using $\delta_T \sim x_T^{0.8}$, where δ_T is the thermal boundary-layer height and x_T is the streamwise distance from a step change in heat flux at the wall [19].

Particle image velocimetry (PIV) was used to acquire streamwise and wall-normal velocity data from a turbulent boundary layer at measurement location D in Fig. 1a. An image of the experiment showing the PIV camera is shown in Fig. 1b. The flow was seeded with bis(2-ethylhexyl)sebacate (also known as DEHS) with a modal size of 0.25 μm, using the LaVision aerosol generator (model no. 1108926). A double-pulsed YLF laser with a frequency of 1.5 kHz and a pulse separation of 35 μs was used to illuminate the flow in the wall-normal streamwise plane. Images were recorded with a Photron Fastcam APX-RS camera with a 17 mm Tamron macrolens at a resolution of

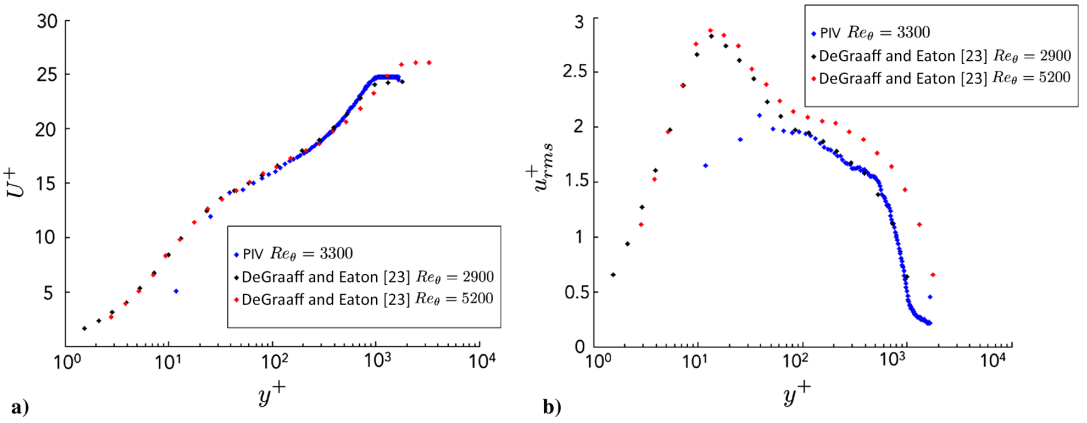

Fig. 3 Velocity statistics: a) mean, and b) rms. Both compared to DeGraaff and Eaton [23].

Downloaded by UNIVERSITY OF NOTRE DAME on July 5, 2019 | http://arc.aiaa.org | DOI: 10.2514/1.J058088

1024×1024 pixels. The field of view was $1.4\delta \times 1.7\delta$ (50×60 mm). DaVis software from LaVision was used to process the data, using a double-pass approach with windows of first 32 and then 16 pixels with 50% overlap [22]. The resolution per vector was 0.013×0.013 outer units or 14.5×14.5 inner units. The Reynolds number was $Re_\theta \equiv U_\infty \Theta/\nu = 3300$ or $Re_\tau \equiv u_\tau \delta/\nu = 910$ at the measurement location in Fig. 1a. The Mach number was 0.05. The 99% boundary-layer thickness δ was found to be 35 mm in the center of the measurement, with a change of 6.7% over 1.7δ of the streamwise extent. The statistics of the velocity field are shown in Fig. 3. The PIV data are shown in blue in Fig. 3 and compared against data from DeGraaff and Eaton [23] at two similar Reynolds numbers. Agreement is seen above $y^+ = 40$ or $y/\delta = 0.04$. Below that height, glare from the PIV laser impinging on the wall affected the quality of the images.

A Malley probe [6,24] was used at measurement location D to measure the local aero-optic distortion. The Malley probe consists of two 1-mm-diameter laser beams aligned in the streamwise direction. In this work, a single beam from a 633 nm JDSU helium neon laser (1145 P, 21 mW, linear polarized) was passed through a spatial filter before it was split into two equal beams by a beam splitter. The beams were then passed through the flowfield along the wall-normal direction, as in Fig. 1c. After passing through the flowfield once, the beams hit a mirror and passed back down through the flow a second time along the same path to increase the strength of the final signal. The beam deflections were sufficiently small (the final beam angle had a standard deviation of 9.5 μrad) that the double-pass approach used in this implementation of the Malley probe measured the effect of the same flow phenomena in both passes. Finally, each beam impinged on a two-dimensional lateral effect position sensor (Thorlabs PDP90A) that identified its centroid position using a T-Cube position sensing detector autoaligner (Thorlabs TQD001). The centroid position was recorded with a sampling rate of 30 kHz. The mean centroid position was arbitrary, depending on the calibration of the setup, but the fluctuation of the centroid position was dependent on the index of refraction field, which was time varying when the beam passed through variable-density flow, due to a relationship between the index of refraction n and density ρ:

$$n(x, y, z, t) = 1 + K_{\mathrm{GD}}\rho(x, y, z, t) \tag{1}$$

where K_{GD} is the Gladstone–Dale constant, and ρ is the density field [25]. The fluctuation of the centroid position was used to deduce the time-varying final angle of each optical beam. An exaggerated schematic of the beam bend and centroid displacement is shown in Fig. 1d with an index of refraction change due to a density gradient event modeled as a step change in density occurring at a point along the beam path.

The beam was deflected in both the streamwise and spanwise directions, and both final angles were measured. This work focused on the streamwise angle. The standard deviation of the final streamwise angle $\theta(t)$ was found to be $\sigma = 9.5$ μrad, and the skewness of the signal was found to be -0.22. Positive values of θ were used to denote downstream inclinations relative to the vertical, whereas negative values of θ denoted upstream inclinations, as indicated in Fig. 1d. Note that the power spectrum of the Malley probe signal in this experiment matched the Malley probe power spectra from other studies at various Reynolds numbers and Mach numbers [20].

III. Modeling

A. Beam Deflection Relationship to the Density Field

The relationship between the angle of the outgoing beam and the local density field can be obtained analytically by making a few assumptions. For a step change in the index of refraction, one generally uses Snell's law to identify the relationship between index of refraction and the angle of a beam. For a continuous change in the index of refraction in a field, one can use a more general description to identify the relationship between the index of refraction of the medium and the angle of the beam locally [26]. First, define the optical path length of a beam of light as

$$S = \int_s n \, \mathrm{d}s$$

where $ds = \sqrt{dx'^2 + dy'^2 + dz'^2}$, and primes indicate parameterized coordinates along the beam path [2]. Additionally, define a single parameterization variable ζ such that $x' = x'(\zeta)$, $y' = y'(\zeta)$, and $z' = z'(\zeta)$. The optical path length is a measure of how many wavelengths the light has gone through as it passes through physical space. Let us also define an optical momentum $\boldsymbol{p}$ as a vector that is everywhere tangent to the ray of light and has magnitude equal to the local index of refraction. One can show that $\boldsymbol{p} = \nabla S$. The streamwise component of the optical momentum vector can be written as $p_x = n(\zeta)\sin(\theta(\zeta))$, where θ is the angle of the ray in the streamwise direction measured with respect to the vertical. Putting these relationships together, we arrive at

$$p_x(\zeta) = n(x'(\zeta), y'(\zeta), z'(\zeta))\sin\theta(\zeta) = \frac{\partial}{\partial x'}S(\zeta) \tag{2}$$

Assuming that all angles that the beam makes with respect to the vertical are small, and using the relationship between the index of refraction and the density highlighted in Eq. (1), one finds

$$\theta(y_f, t) - \theta(y_i) \approx K_{\mathrm{GD}} \int_{y_i}^{y_f} \frac{\partial \rho}{\partial x}(x_i, y, z_i, t)\, \mathrm{d}y \tag{3}$$

where $\theta(y_f, t)$ is the time-varying final streamwise angle of the beam, $\theta(y_i)$ is the incoming angle of the beam, and x_i and z_i are the incoming streamwise and spanwise locations of the beam.

B. Coherent Velocity Structure Representation

A simple model for coherent large-scale velocity structures is considered in which periodic traveling waves are used as a basis to represent the flowfield. These traveling waves take the form of

$$\tilde{\boldsymbol{u}} = \hat{\boldsymbol{u}}_K(y)\exp(i(k_x x + k_z z - \omega t)) \tag{4}$$

where $\hat{\boldsymbol{u}}_K$ represents the wall-normal coherence at a specific set of streamwise and spanwise wave numbers (k_x and k_z) and a temporal

Downloaded by UNIVERSITY OF NOTRE DAME on July 5, 2019 | http://arc.aiaa.org | DOI: 10.2514/1.J058088

frequency ω. Note that this representation does not account for the growth of the boundary layer in the streamwise direction; one could do so using more computationally intensive methods, including with a two-dimensional representation of the modal shape. The use of a traveling wave as a model for coherent structures is consistent with spectral descriptions of turbulence, in which particular wave numbers are observed to be energetic in premultiplied energy spectra.

To create a model of a representative scale in this framework, one specifies the scale of interest through k_x, k_z, and ω; and one identifies a representation of the wall-normal coherence $\hat{\boldsymbol{u}}_K$. In this study, because the velocity data available from experiments are only in the streamwise/wall-normal plane, the spanwise behavior of the model is not relevant and k_z can be set to zero for simplicity. The values of $k_x\delta = (\pi/2)$ and $\omega(\delta/U_\infty) = (1/5)$ used here were identified from statistics in the literature as characteristic values for a large-scale motion in turbulent boundary layers [8,27]. To estimate the wall-normal coherence $\hat{\boldsymbol{u}}_K(y)$, one can determine the wall-normal coherence that is most amplified by the linear dynamics of the Navier–Stokes equations using a resolvent analysis, as was done by McKeon and Sharma [28], Sharma and McKeon [29], and McKeon [30]. A traveling-wave model with the wave numbers identified for large-scale motions, a specified spanwise wavelength, and a coherence defined using a resolvent analysis was described by Saxton-Fox and McKeon [31] and shown to demonstrate structural similarity to realistic flows in visualizations and in analyses of uniform momentum zones.

Here, the form of $\hat{\boldsymbol{u}}_K$ is left as essentially an unknown. The only information that is used here is that the structure is active (has a nontrivial amplitude) at the height in the flow where the mean velocity is equal to the wave speed of the structure: i.e., the critical layer y_c, where $\bar{U}(y_c) = c$. The assumption of a nontrivial amplitude of the model at the critical layer is consistent with Taylor's hypothesis and is supported by the work of McKeon and Sharma [28], which demonstrated that high amplification associated with the linear dynamics of the Navier–Stokes equations was concentrated at the critical layer for a given wave and that there was a concentration of critical layers, which is in contrast to linear stability theory.

In this work, the density and index of refraction fields are not quantitatively modeled but are instead qualitatively deduced from an analysis of experimental data. However, one can create such a model using either a strong Reynolds analogy applied instantaneously, as was done by Gordeyev et al. [5], or using a resolvent analysis performed on the Navier–Stokes equations and the passive scalar equation [12].

IV. Analysis Methods

A. Conditional Statistics

Conditional averaging and a conditional standard deviation were used to investigate the relationship between beam deflections and velocity features. Beam deflections and the velocity field should be related through the velocity field's effect on the passive scalar field, which in turn affects the index of refraction field through Eq. (1). For a boundary layer with a passive scalar source at the wall and $Pr = 0.71$, one would expect the density field to behave somewhat similarly to the streamwise velocity field, although with increased diffusion from Prandtl number effects and other velocity-scalar differences mentioned in the Introduction (Sec. I). The relationship between the scalar field and the velocity field as well as the relationship between density gradients and the Malley probe approximated in Eq. (3) together indicate that one would expect velocity gradients to be correlated to beam deflection. Three variations on conditional statistics were used to probe this relationship and its dependence on particular velocity structures.

1. *First Condition: Beam Deflection*

The first conditional statistic used a condition based upon the beam deflection signal to average the velocity field. For this case, velocity data were averaged when the absolute value of the beam deflection angle was larger than half of its standard deviation: $\theta(t) > (1/2)\sigma$ or $\theta(t) < -(1/2)\sigma$. This condition identified velocity structures correlated to large upstream or downstream beam deflections. The upstream conditional averages considered in the first variation were

$$\left\langle u, v|_{\theta<-\sigma/2} \right\rangle \tag{5}$$

and the downstream conditional averages were

$$\left\langle u, v|_{\theta>\sigma/2} \right\rangle \tag{6}$$

For shorthand, the first conditional averaging variation for some quantity Q was written as

$$\langle Q|_\theta \rangle \tag{7}$$

to indicate that the condition was based on the beam deflection.

2. *Second Condition: Phase of Large-Scale Motion*

The second variation of conditional statistics in this study used a condition based upon the velocity field. The goal of this second variation was to identify the variation in the beam deflection behavior as a function of the presence and position of a large-scale motion in the flow. This variation used a projection condition to identify the presence and position of the large-scale motion. A standard deviation was used rather than an average to identify the variation in beam deflection behavior because the fluctuation of the aero-optic signal was the focus of the study rather than its average behavior.

For the condition, the model of a large-scale motion described in Sec. III.B was compared to instantaneous data of the fluctuating

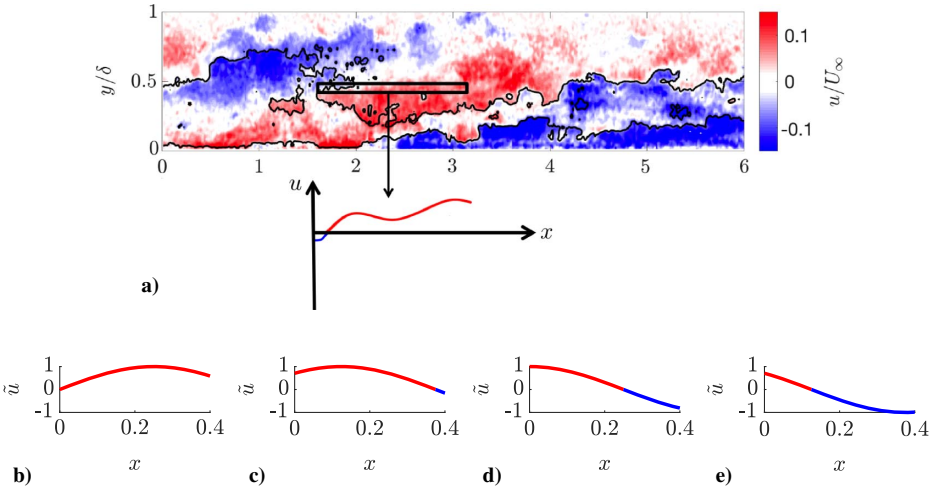

Fig. 4 Projection method schematic: a) data extracted, and b) model at four phases.

Downloaded by UNIVERSITY OF NOTRE DAME on July 5, 2019 | http://arc.aiaa.org | DOI: 10.2514/1.J058088

streamwise velocity field from the experiment at the height y_c, which is the critical layer height of the model. This is schematically demonstrated in Fig. 4 with four phases instead of eight for image clarity. Fluctuating streamwise velocity data were extracted at a single height (corresponding to the critical layer height of the large-scale motion model) from the measurement field, represented in Fig. 4a, and they were compared against the model of the fluctuating velocity field with four starting phases, represented in Fig. 4b. Note that the velocity data shown in Fig. 4a are an extended visualization created by convecting the particle image velocimetry data with a fixed convection velocity of $0.8U_\infty$, following Zaman and Hussain [32]. This is done purely for visualization purposes, and it is not done within the analysis. The extracted data in Fig. 4a are representative of the field of view of the measurement.

The comparison between the model and the extracted data was carried out using a projection:

$$R(\gamma, t) = \frac{u(x, y_c, t) \cdot \tilde{u}(x, y_c, t + 2\pi(\gamma/N)\omega t)}{|u(x, y_c, t)||\tilde{u}, (x, y_c, t + 2\pi(\gamma/N)\omega t)|} \tag{8}$$

where u is the fluctuating streamwise velocity field, and $\tilde{u}$ is the model of the large-scale motion. The value of γ was varied between one and the total number of phase windows considered ($N = 8$), allowing for the identification of the structure as it convected downstream. The maximum value of R over the varied γ was identified, and the phase at which the maximum occurred was recorded:

$$R^*(t) = \max_\gamma R(\gamma, t) \tag{9}$$

and

$$\gamma^*(t) = \arg\max_\gamma R(\gamma, t) \tag{10}$$

In the visualization of the method, shown in Fig. 4, a comparison of the extracted data with the sine wave at different phases would identify that the extracted data were most similar to the first of these phases, such that $\gamma^*(t_0) = 1$, and that the projection between the two had some projection coefficient $R^*(t_0)$. If R^* was larger than a threshold value R_{th}, then it was concluded that a structure had been identified at the given time snapshot, sitting at a phase γ^*. Statistics were then calculated for the group of data associated with each phase. For some quantity Q, the conditional average would be written as

$$\left\langle Q|_{R^*>R_{\text{th}}} \right\rangle^{\gamma^*} \tag{11}$$

for each phase, resulting in N averages. In this case, the conditional standard deviation was considered and written as

$$\sigma\left(Q|_{R^*>R_{\text{th}}} \right)^{\gamma^*} \tag{12}$$

for each phase, resulting in N standard deviations. The variable Q was conditioned on the value of R^*, which is the maximum projection coefficient; and the conditional statistics were calculated with other values of Q that had the same value of γ^*.

The projection condition identified the phase that best represented where the local large-scale velocity signature was in its convection through the field of view. However, because the field of view in this study was smaller than the wavelength of a large-scale motion, the projection condition did not exclusively permit structures with the chosen wavelength λ_x to be included in the ensuing statistics. Because the field of view was smaller than the streamwise wavelength of the desired structure, the projection condition acted similarly to a low-pass filter, averaging on the location of any large scales with a wavelength greater than 2δ active at the chosen height y_c and time t of the snapshot. With larger fields of view, the projection would act more and more similarly to a bandpass filter: only averaging when a structure with a streamwise wavelength near the wavelength of the model was identified. This is shown in Fig. 5 using a toy problem in which the model is a sine wave $\tilde{u} = \sin(\tilde{\lambda}x)$ with $\tilde{\lambda} = 1$ and the velocity field is a sine wave with a wavelength that is allowed to vary between 0.1 and 2: $u = \sin(\lambda x)$. The field of view is varied between $\Lambda = 0.4$ (Fig. 5a), 1 (Fig. 5b), and 2 (Fig. 5c). The maximum projection coefficient across the phases R^* is shown to be fairly constant above a threshold wavelength in Fig. 5a, acting as a low-pass filter in frequency; whereas it falls off at other wavelengths in Figs. 5b and 5c as the field of view is increased, acting as a bandpass filter. The ratio of the field of view to the wavelength of the model in this study is similar to that of Fig. 5a.

Statistically, in turbulent wall-bounded flows, large-scale motions are energetically dominant at the height y_c that is chosen in this study and are somewhat broad in their frequency content, containing energy between 2 and 5δ [8]. As shown in Fig. 5, the projection condition acts similarly to a low-pass or bandpass filter, depending on the field of view of the data. Because the projection was carried out at the height at which large-scale motions are dominant, we argue that the method primarily averaged on large-scale motions. A benefit of the low-pass behavior of the method is that it allows the full family of large-scale motions to be included across the 2–5δ streamwise wavelength peak. Increasing the field of view of the data would permit fewer considered wavelengths.

The sampling frequency for the Malley probe was higher than that of the PIV; so, to maximize the amount of data that could be efficiently used in the statistics, the beam deflection signal was binned into temporal bins $\theta(\tau)$ with

$$\boldsymbol{\tau} = t - \frac{\Delta t_{\text{PIV}}}{4} : t + \frac{\Delta t_{\text{PIV}}}{4} \tag{13}$$

Here, Δt_{PIV} is the time between samples in the PIV data and t is the time at which each PIV sample is taken. The second variation on conditional statistics was therefore

$$\sigma\left(\theta(\tau)|_{R^*>R_{\text{th}}} \right)^{\gamma^*} \tag{14}$$

The condition is on the value of R^*, which is the maximum projection coefficient; and the statistics are taken together with all values of the beam deflection associated with the same value of γ^*. Note that this will lead to eight different values of the standard deviation: one for each phase of the large-scale motion γ. For shorthand, this conditional standard deviation for some quantity Q will be labeled

$$\sigma(Q|u) \tag{15}$$

to denote that the condition is based on the fluctuating streamwise velocity field.

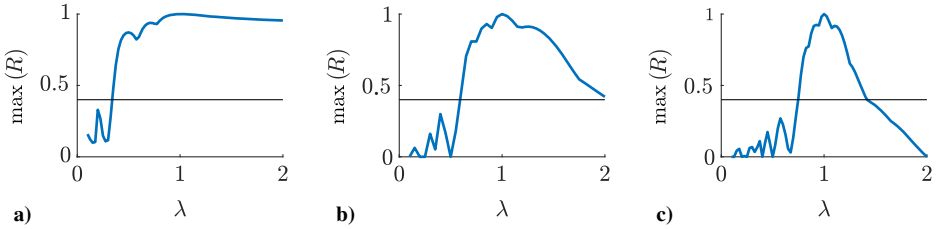

Fig. 5 Maximum projection coefficient for toy problem. Projection length is a) 0.4, b) 1, and c) 2. The black line shows $R_{\text{th}} = 0.4$.

3. Third Condition: Beam Deflection and Phase of Large-Scale Motion

The third conditional statistic was conditioned on both the beam deflection signal and the velocity field. In this case, data were averaged when the beam deflection angle was larger in magnitude than half its standard deviation [$|\theta(t)| > \sigma/2$] and the velocity projection value was larger than a threshold [$R^*(t) > R_{\text{th}}$]. The conditional averages using this variation were

$$\left\langle u, v, u_s, v_s|_{(\theta<-\sigma/2, R^*>R_{\text{th}})}\right\rangle^{\gamma^*} \tag{16}$$

for upstream beam deflections and

$$\left\langle u, v, u_s, v_s|_{(\theta>\sigma/2, R^*>R_{\text{th}})}\right\rangle^{\gamma^*} \tag{17}$$

for downstream beam deflections, where u_s and v_s are small-scale streamwise and wall-normal velocity fields, which are defined using a Gaussian filter. For a quantity Q, the conditional average was written as

$$\langle Q|_{\theta,u}\rangle \tag{18}$$

to indicate that the two conditions were based on the beam deflection and the streamwise velocity field. This technique led to eight different averaged velocity fields per variable: one for each phase of the modeled large scale γ. These separate images were stitched together in order to consolidate the information, leading to final images in which the beam deflection appears to be measured in eight separate locations.

B. Filtering

A Gaussian filter was used to identify small-scale velocity features in order to study the effect on the beam deflection of scales smaller than large-scale motions. The small-scale features were defined as the remainder of a convolution of the fluctuating velocity field with a Gaussian kernel. The convolution was normalized by the integral of the Gaussian kernel to minimize edge effects:

$$u_s(x,y,t) = u(x,y,t) - \frac{\int_{x_j^*}^{x_f^*}\int_{y_i^*}^{y_f^*} u(x^*,y^*,t)\exp(-(((x-x^*)^2+(y-y^*)^2)/(2\sigma_G)^2))\,\mathrm{d}x^*\,\mathrm{d}y^*}{\int_{x_j^*}^{x_f^*}\int_{y_i^*}^{y_f^*}\exp(-(((x-x^*)^2+(y-y^*)^2)/(2\sigma_G)^2))\,\mathrm{d}x^*\,\mathrm{d}y^*} \tag{19}$$

$$v_s(x,y,t) = v(x,y,t) - \frac{\int_{x_j^*}^{x_f^*}\int_{y_i^*}^{y_f^*} v(x^*,y^*,t)\exp(-(((x-x^*)^2+(y-y^*)^2)/(2\sigma_G)^2))\,\mathrm{d}x^*\,\mathrm{d}y^*}{\int_{x_j^*}^{x_f^*}\int_{y_i^*}^{y_f^*}\exp(-(((x-x^*)^2+(y-y^*)^2)/(2\sigma_G)^2))\,\mathrm{d}x^*\,\mathrm{d}y^*} \tag{20}$$

The standard deviation of the Gaussian was $\sigma_G = 0.5\delta$, which gives an approximate cutoff wavelength of the filter as $\lambda_G/\delta = 2.7$.

V. Results

First, the velocity field was conditionally averaged on the beam deflection angle. Figure 6 shows the result of this averaging for the streamwise velocity field (Figs. 6a and 6c) and the wall-normal velocity field (Figs. 6b and 6d) for upstream (Figs. 6a and 6b) and downstream (Figs. 6c and 6d) beam deflections. The Malley probe passes vertically through the flow at $\hat{x} = 0$ in the images. The number of frames used to calculate the results in Fig. 6 is shown in Table 1.

In all cases in Fig. 6, a velocity gradient is observed at the Malley probe location, which is observable as a change in the sign of the fluctuating velocity field. In the streamwise velocity field (Figs. 6a and 6c), this gradient is of the same sign as the density gradient implied by the sense of beam deflection such that

$$\frac{\partial u}{\partial x} \approx \frac{\partial \rho}{\partial x}$$

whereas in the wall-normal velocity field (Figs. 6b and 6d), the gradient has the opposite sign as the associated density gradient of the beam deflection:

$$\frac{\partial v}{\partial x} \approx -\frac{\partial \rho}{\partial x}$$

To isolate the effect of the large-scale motions on the beam deflection signal, the velocity projection condition was used. The Malley probe signal $\theta(t)$ was averaged if a large-scale motion was identified at a particular phase in the corresponding PIV snapshot. The variation in the standard deviation of the Malley probe signal as a function of the large-scale motion phase is shown in Fig. 7a. The value of the large-scale motion model at the Malley probe streamwise location is shown in Fig. 7b for reference.

The standard deviation of the Malley probe signal was observed to vary by 11%, depending on the local sign of the large-scale streamwise velocity fluctuation. The maximum standard deviation occurred at the transition between the positive and negative streamwise velocity features, which correspond to a shear-layer region. The standard deviation was, in general, larger when the streamwise velocity's fluctuating amplitude was negative than when it was positive. The number of frames and data points used to calculate the statistics in Fig. 7 across the phases is given in Table 2. The convergence of the statistics was investigated by decreasing the number of PIV frames considered. The 20 and 40% reductions in the number of frames considered led to maximum changes in the standard deviations over all phases of 1.2 and 2.8%, respectively.

The standard deviation of the beam deflection signal did show some sensitivity to the phase of a passing large-scale motion, but the sensitivity was fairly low (10%). Thus, it was of interest to identify other velocity features that appeared concurrently with the large-scale motion during significant beam deflection. Figures 8 and 9 show the result of conditionally averaging the velocity field on both the beam deflection and on the presence of a large-scale motion. The streamwise (Figs. 8a and 9a), wall-normal (Figs. 8b and 9b), small-scale streamwise (Figs. 8c and 9c), and small-scale wall-normal (Figs. 8d and 9d) fluctuating velocity fields are shown for upstream deflections (Fig. 8) and downstream deflections (Fig. 9).

The number of frames used to calculate the results in Figs. 8 and 9 is shown in Table 3. Table 4 provides more detailed information, showing the number of frames used to calculate the conditional average at each phase separately. Each panel shows eight separate conditional averages, performed for each phase γ^* of the large-scale motion, stitched together for ease of visualization. The streamwise coordinate is defined as

$$x^\gamma = \hat{x} + \lambda_x\left(\frac{\gamma - 1/2}{N}\right)$$

where λ_x is the streamwise wavelength of the large-scale motion, $\hat{x}$ is the streamwise coordinate with $\hat{x} = 0$ centered at the Malley probe measurement location, and N is the number of phases considered. The $(1/2N)$ term allows $x^\gamma = 0$ to occur at the farthest upstream

Downloaded by UNIVERSITY OF NOTRE DAME on July 5, 2019 | http://arc.aiaa.org | DOI: 10.2514/1.J058088

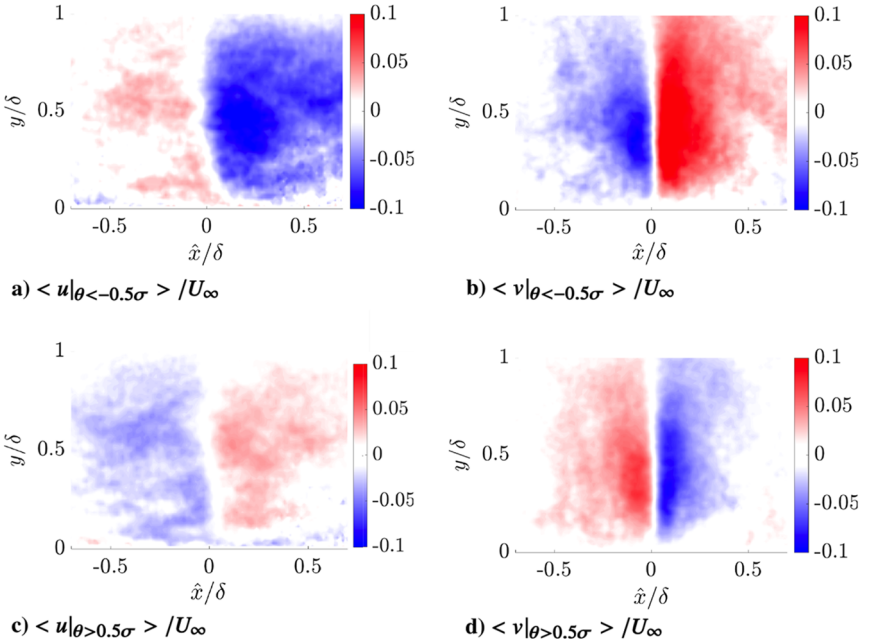

Fig. 6 Average velocity fields conditioned on beam deflection at $\hat{x} = 0$.

location in the visualization rather than coinciding with the first dashed line. For a large-scale motion, this coordinate system shows a full period of the structure, given equidistant spacing of the phases across $[0, 2\pi)$. For the structures correlated to the Malley probe, this visualization allows for eight views of the structural behavior, depending on the phase of the large-scale motion.

In Figs. 8a and 9a, the averaged, fluctuating streamwise velocity field $\langle u|_{\theta,u}\rangle/U_\infty$ demonstrates behavior consistent with the projection conditional averaging technique: the output is periodic, as the model is, with a streamwise wavelength of 4δ. The structure shows an inclination downstream. The averaged, fluctuating wall-normal velocity field $\langle v|_{\theta,u}\rangle/U_\infty$ (Figs. 8b and 9b) shows a relationship to the streamwise velocity field that is consistent with Reynolds stresses: negative wall-normal velocity is associated with positive streamwise velocity. Some behavior is observed, however, that does not appear to be directly correlated to the streamwise velocity features. In the upstream deflection case (Fig. 8b), a positive streamwise gradient is observed near the dashed lines, whereas in the downstream deflection case (Fig. 9b), a negative streamwise gradient is observed at the dashed lines. More than one scale appears in the wall-normal velocity fields.

The small-scale velocity fields shown in Figs. 8 and 9 are defined in Eqs. (19) and (20). In the streamwise small-scale fields $\langle u_s|_{\theta,u}\rangle/U_\infty$, inclined alternating-signed structures are observed. The signature of specific flow events at the beam locations is fairly weak, although a very mild negative streamwise gradient can be deduced from the upstream deflection case (Fig. 8c) at many of the black dashed lines.

In the small-scale wall-normal field $\langle v_s|_{\theta,u}\rangle/U_\infty$, shorter upright structures are observed (Figs. 8d and 9d). These structures consistently change sign across the dashed line, where the Malley probe passes through the flow. The sense of the sign change is observed to differ between Figs. 8d and 9d: moving downstream across the dashed lines, the wall-normal small scales vary from negative to positive in Fig. 8d and vary from positive to negative in Fig. 9d.

Table 1 Frames used for the results of Fig. 6

	$\theta < -\sigma/2$	$\theta > \sigma/2$
Number of frames	2262	3675
Percentage of frames	22	36

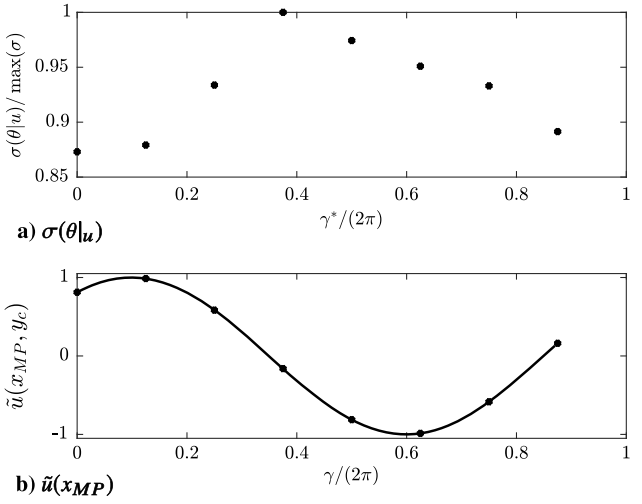

Fig. 7 Standard deviation of the beam, conditioned on the phase of the large-scale motion (Fig. 7a), and the value of the large-scale motion model locally (Fig. 7b).

The change in sign in the small-scale wall-normal velocity field is relatively consistent across the phases of the large-scale motion within each image (Figs. 8d and 9d). One change that is observed in the wall-normal event is a slight shift in the height at which the event occurs. This is most easily seen in Fig. 8d, in which the small scales at a value of $x/\delta \approx 0$ sit near a value of $y/\delta \approx 0.25$, whereas the small scales at a value of $x/\delta \approx 4$ sit near a value of $y/\delta \approx 0.5$. This change in height is consistent with previous observations of a correlation between the spatial organization of small-scale structures and the local sign of large scales [33,34]. In the downstream deflection case (Fig. 9d), localization near the wall is observed at values of $x/\delta \approx 1$, but less clear coherence is observed in the small scales around $x/\delta \approx 4$.

VI. Discussion

A velocity gradient, particularly pronounced in the wall-normal velocity field, was observed to be highly correlated with the deflection of an optical beam passing through the heated, turbulent flow. When the velocity field was only averaged on the beam deflection condition, as in Fig. 6, this gradient appeared consistently

Downloaded by UNIVERSITY OF NOTRE DAME on July 5, 2019 | http://arc.aiaa.org | DOI: 10.2514/1.J058088

Table 2 Data used to calculate the statistics in Fig. 7

	Phase γ							
	0	1/8	1/4	3/8	1/2	5/8	3/4	7/8
Number of PIV frames	632	557	678	622	627	557	653	625
Number of beam deflection data points	25,912	22,837	27,798	25,502	25,707	22,837	26,773	25,625
Percentage of total data	12	11	13	12	12	11	13	12

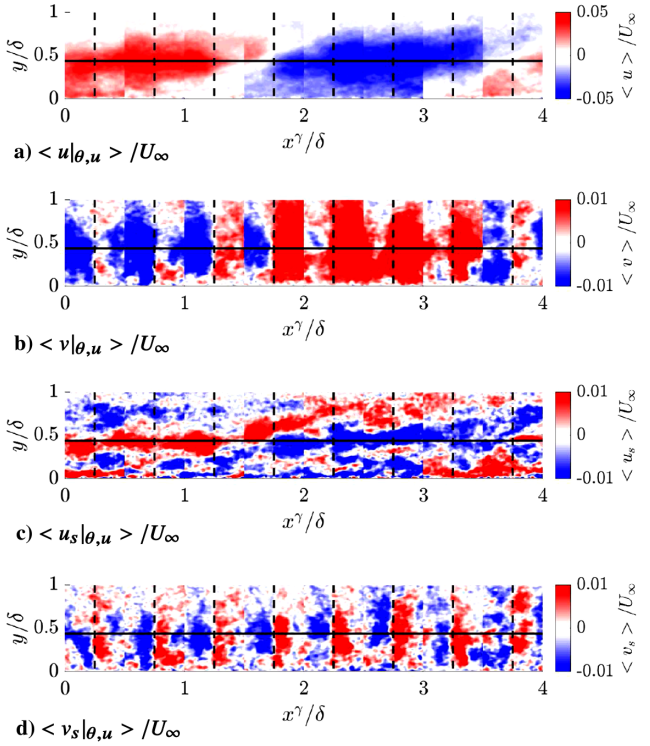

Fig. 8 Conditional averages using the combined condition with upstream Malley probe deflection.

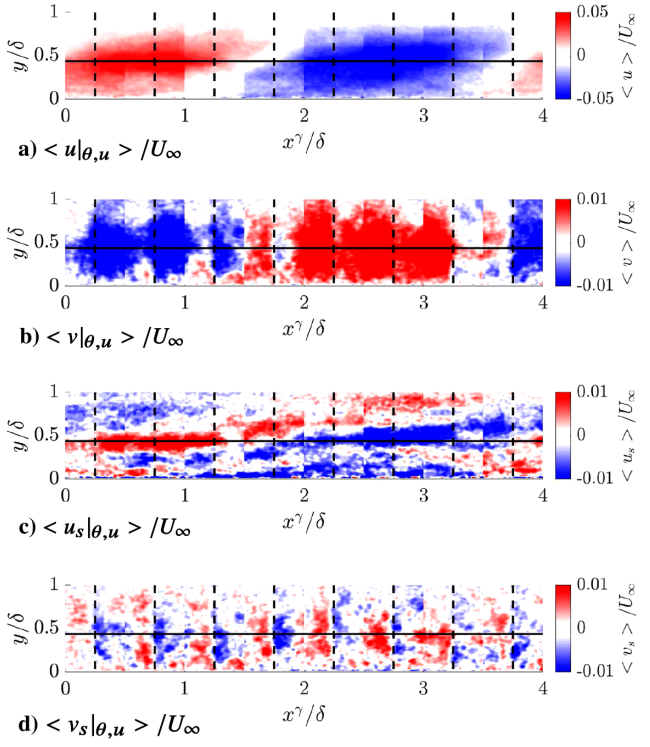

Fig. 9 Conditional averages using the combined condition with downstream Malley probe deflection.

through the full height of the flow. The interpretation of this result is complicated by the integral nature of the optical measurement: events happening throughout the height of the boundary layer could affect the deflection of the beam. Toward unraveling the velocity features that affect the beam deflection, the beam deflection signal was conditioned on the phase of a passing large-scale motion, which was defined using a traveling-wave model of coherent structures. Depending on the large-scale motion phase, the standard deviation of the beam deflection varied by about 10%, indicating that the large-scale motion had some significance to the beam deflection.

When the phase of the large-scale motion was fixed using the projection conditional averaging method, a streamwise gradient at the Malley probe location was observed in the wall-normal velocity field, particularly in the small-scale field, but was not consistently observed in the streamwise velocity field (Figs. 8a and 9a). Some evidence of a streamwise gradient was observed in the small-scale streamwise velocity field conditioned on an upstream deflection (Fig. 8c), but little evidence of a streamwise gradient at the beam location was observed in the downstream deflection case (Fig. 9c).

Most of the behavior in the small-scale streamwise velocity fields in Figs. 8c and 9c $u_s|_{\theta,u}$ was not significantly correlated to the beam deflection signal. This could be concluded by comparing Figs. 8c and 9c: little change was observed in the behavior although the beam deflection was of the opposite sense. The small-scale streamwise velocity was also investigated using the projection condition without the beam deflection condition, and a similar averaged field was observed. The long inclined structures were therefore primarily associated with the projection condition rather than with the beam deflection condition. The structure of the small-scale streamwise velocity field, dominated by an inclined high-speed region lying atop a low-speed region, suggested the presence of a shear layer (Figs. 8c and 9c). Shear layers have been associated with the backs or edges of bulges and uniform momentum zones by many researchers [10,35–37]. Both bulges and uniform momentum zones were argued to be consistent with the presence of large-scale motions by Saxton-Fox and McKeon [31]. In this case, by conditioning on the presence of a large-scale motion, the small-scale streamwise velocity field was dominated by the associated shear layers. These findings do not necessarily suggest that streamwise small-scale motions are uncorrelated to beam deflections; rather, they indicate that the features of the large-scale motion largely overpower other correlations that might exist.

The small-scale wall-normal velocity fields conditioned on both the beam deflection and the projection condition $v_s|_{\theta,u}$ showed the most consistent relationship with the Malley probe signal: it retained the appropriately signed gradient, regardless of the large-scale motion phase. The gradient observed in the small-scale wall-normal field (Figs. 8d and 9d) was consistent in strength and size, but it was more localized in the wall-normal direction than in Fig. 6, and it appeared to sit at different heights, depending on the phase of the large-scale motion. The consistency of the strength of the wall-normal velocity gradient may explain the reasonable consistency (within 10%) of the standard deviation of the beam deflection signal across the phases of the large scale.

Table 3 Data used for the results of Figs. 8 and 9

	$\theta < -\sigma/2$	$\theta > \sigma/2$
Number of frames	1420	1637
Percentage of frames	28	32

Downloaded by UNIVERSITY OF NOTRE DAME on July 5, 2019 | http://arc.aiaa.org | DOI: 10.2514/1.J058088

Table 4 Data per phase in Fig. 8 ($\theta < -\sigma/2$) and Fig. 9 ($\theta > \sigma/2$)

	Phase ($\gamma/2\pi$)							
	0	1/8	1/4	3/8	1/2	5/8	3/4	7/8
Number of frames $\theta < -\sigma/2$	271	188	119	120	282	208	104	128
Number of frames $\theta > \sigma/2$	315	220	123	172	303	218	119	166
Percentage of frames $\theta < -\sigma/2$	5	4	2	2	6	4	2	2
Percentage of frames $\theta > \sigma/2$	6	4	2	3	6	4	2	3

These findings motivated a hypothesis regarding the role of large and small scales in affecting the optical signal. In this hypothesis, schematically shown in Fig. 10, the large scale is primarily responsible for carrying the heat, whereas the small scales create localized gradients that affect the optical signal. The deduced thermal behavior is shown in Fig. 10: slower large-scale streamwise areas are warmer, whereas faster areas are cooler [38]. The small-scale wall-normal features sit at a variable height from the wall, depending on the large-scale phase. They transport warm or cool air across the boundary of the large scale and are thermally associated with the side of the boundary from which their arrow starts. Note that, on average, the freestream is cool, whereas flow near the wall is warm. Note also that the conceptual model illustrated in Fig. 10 assumes a Prandtl number near one, where velocity structures have a similar coherence as scalar structures. In nonunity Prandtl number flows, the scalar structures may appear much more diffuse or much more concentrated than the velocity structures, modifying the representations in Figs. 10 and 11.

Cyan stars in Fig. 10 indicate locations where an upstream optical beam deflection would be expected because the small scales create a local $+\partial T/\partial x$ event or, equivalently, a local $-\partial\rho/\partial x$ event. Orange diamonds indicate locations where a downstream optical beam deflection would be expected because the small scales create a local $-\partial T/\partial x$ event or, equivalently, a local $+\partial\rho/\partial x$ event.

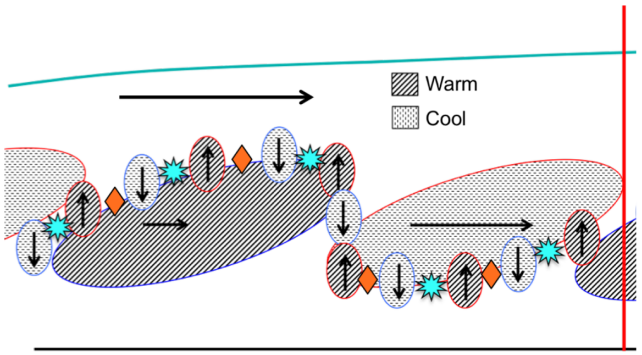

Fig. 10 Hypothesized scalar transport. Cyan stars show upstream beam deflection events, and orange diamonds show downstream beam deflection events.

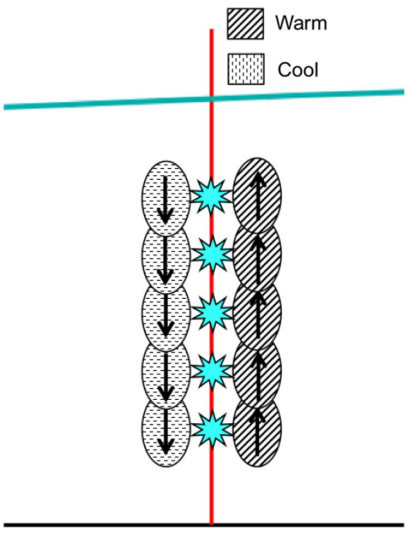

Fig. 11 Multiple wall-normal velocity events associated with upstream Malley probe deflection: superimposed.

This hypothesis is consistent with the hairpin packet structure of the boundary layer discussed in Refs. [10,39]; the small-scale wall-normal structures overlaid with a streamwise velocity gradient are equivalent to hairpin vortex heads sitting above regions of low-speed fluid in the left half of Fig. 10. In the hairpin vortex perspective, the orange diamonds corresponding to downstream optical beam deflection events are coincident with hairpin vortex heads, whereas the cyan stars where upstream optical deflection events occur are coincident with stagnation points between neighboring hairpin vortices. This hypothesis is consistent with data from a uniformly sheared turbulent flow, in which hairpin vortices were correlated to scalar flux events [18].

In the conceptual model in Fig. 10, the events that would trigger large Malley probe deflections occur throughout the flow height. When conditionally averaging only on the beam deflection, all of these events would be equally considered, leading to a superposition of structures as shown in Fig. 11. Multiple wall-normal velocity features are shown, associated with warm or cool air, depending on the sense of the density gradient implied by the beam deflection measurement, and stacked in the wall-normal direction to create what appears to be a single, tall gradient. This offers an interpretation of the results in Fig. 6: the tall gradients are perhaps the result of averaging multiple smaller structures, sitting at a variety of heights rather than representative of a single structure.

Although this study was performed at a relatively low Reynolds number and in incompressible flow, there is evidence that similar scales are relevant for the aero-optic signal at much higher Reynolds numbers and Mach numbers. Data at even lower Reynolds numbers from this facility were compared with data at $Re_\theta = 20{,}000$ and $M = 0.41$, and the aero-optic deflection angle spectrum was observed to collapse when plotted against $St_\delta = f\delta/U_\infty$ [20]. The only exception to the collapse occurred at high frequencies, where the falloff was faster at lower Reynolds numbers.

The findings of this work motivate the study of very-reduced-order models, perhaps as simple as a single large scale and a single small scale, in which the smaller-scale structures sit at variables heights, depending on the large-scale phase, as is qualitatively shown in Fig. 10. The implementation of such a model for both the velocity and scalar fields and the evaluation of its predictive ability for aero-optic applications are topics of ongoing work [40].

VII. Conclusions

An experimental study was carried out to study the distortion of an optical beam passing along the wall-normal direction through a heated, incompressible turbulent boundary layer. Density variation in the air from heating at the wall led to index of refraction variation in the turbulent flow, perturbing the beam deflection angle in time. Simultaneous measurements were undertaken of the beam deflection using a Malley probe and of the velocity field using particle image velocimetry.

Conditional averaging techniques were used to isolate correlations between beam deflection events and velocity field events. A strong relationship was found between beam deflections and streamwise gradient events in both the streamwise and wall-normal velocity fields. The effect of a large-scale motion passing through the beam

Downloaded by UNIVERSITY OF NOTRE DAME on July 5, 2019 | http://arc.aiaa.org | DOI: 10.2514/1.J058088

was isolated using a projection condition and was found to change the standard deviation of the deflection signal by as much as 11%.

In the presence of the large-scale motion at any phase, a streamwise gradient in the small-scale wall-normal velocity field was observed to be consistently correlated to optical distortion. The height at which the gradient was strongest appeared to be correlated to the phase of the large-scale motion, which was consistent with previous findings regarding large- and small-scale phase organization.

A hypothesis was formed from the experimental observations regarding the role of the large and small scales in the transport of heat and the distortion of an optical beam. In the conceptual model, the low-speed large-scale structures carried heat and generated significant thermal gradients along their backs (consistent with the literature [38]). The small scales modified the thermal gradient to create local streamwise gradient events at the boundaries of the large scales. These streamwise gradient events were able to affect the optical system through an index of refraction gradient at an oblique angle to the beam.

To correctly predict the optical aberrations, one would need to predict the large-scale behavior, the location of the small scales relative to the large scales, and the local transport of heat of both the large and small scales. The implementation of such a model is a topic of ongoing work.

Acknowledgments

The support of the U.S. Air Force through grant no. FA9550-12-1-0060 and grant no. FA9550-16-1-0361, as well as the support of the U.S. Department of Defense through a National Defense Science and Engineering Graduate Fellowship (TSF) are gratefully acknowledged. The authors gratefully acknowledge Adam Smith, whose expertise in the Malley probe aided in the development of the experimental setup, as well as Scott Dawson, whose work on modeling the scalar field informed the future work of this project.

References

[1] Liepmann, H. W., "Deflection and Diffusion of a Light Ray Passing Through a Boundary Layer," Douglas Aircraft Company, Santa Monica Division, TR SM-14397, Santa Monica, CA, 1952.

[2] Wang, M., Mani, A., and Gordeyev, S., "Physics and Computation of Aero-Optics," *Annual Review of Fluid Mechanics*, Vol. 44, Jan. 2012, pp. 299–321. doi:10.1146/annurev-fluid-120710-101152

[3] Jumper, E. J., and Gordeyev, S., "Physics and Measurement of Aero-Optical Effects: Past and Present," *Annual Review of Fluid Mechanics*, Vol. 49, Jan. 2017, pp. 419–441. doi:10.1146/annurev-fluid-010816-060315

[4] Dimotakis, P. E., Catrakis, H. J., and Fourguette, D. C., "Flow Structure and Optical Beam Propagation in High-{Reynolds}-Number Gas-Phase Shear Layers and Jets," *Journal of Fluid Mechanics*, Vol. 433, April 2001, pp. 105–134. doi:10.1017/S0022112000003281

[5] Gordeyev, S., Smith, A., Cress, J., and Jumper, E., "Experimental Studies of Aero-Optical Properties of Subsonic Turbulent Boundary Layers," *Journal of Fluid Mechanics*, Vol. 740, Feb. 2014, pp. 214–253. doi:10.1017/jfm.2013.658

[6] Gordeyev, S., Cress, J. A., Smith, A., and Jumper, E. J., "Aero-Optical Measurements in a Subsonic, Turbulent Boundary Layer with Non-Adiabatic Walls," *Physics of Fluids*, Vol. 27, No. 4, 2015, Paper 045110. doi:10.1063/1.4919331

[7] Tyson, R. K., *Principles of Adaptive Optics*, 2nd ed., Academic Press, New York, 1997. doi:10.1201/ebk1439808580

[8] Monty, J. P., Hutchins, N., Ng, H. C. H., Marusic, I., and Chong, M. S., "A Comparison of Turbulent Pipe, Channel and Boundary Layer Flows," *Journal of Fluid Mechanics*, Vol. 632, Aug. 2009, pp. 431–442. doi:10.1017/S0022112009007423

[9] Theodorsen, T., "Mechanism of Turbulence," *Proceedings of the Midwestern Conference on Fluid Mechanics*, Ohio State Univ., Columbus, OH, 1952, https://scholar.google.com/scholar_lookup?hl=en-US&publication_year=1952&author=T.+Theodorsen&title=Mechanism+of+turbulence.

[10] Adrian, R. J., Meinhart, C. D., and Tomkins, C. D., "Vortex Organization in the Outer Region of the Turbulent Boundary Layer," *Journal of Fluid Mechanics*, Vol. 422, Nov. 2000, pp. 1–54. doi:10.1017/S0022112000001580

[11] Ganapathisubramani, B., Longmire, E. K., and Marusic, I., "Characteristics of Vortex Packets in Turbulent Boundary Layers," *Journal of Fluid Mechanics*, Vol. 478, March 2003, pp. 35–46. doi:10.1017/S0022112002003270

[12] Dawson, S., McKeon, B., and Saxton-Fox, T., "Modeling Passive Scalar Dynamics in Wall-Bounded Turbulence Using Resolvent Analysis," *2018 AIAA Fluid Dynamics Conference*, AIAA Paper 2018-4042, 2018. doi:10.2514/6.2018-4042

[13] Warhaft, Z., "Passive Scalars in Turbulent Flows," *Annual Review of Fluid Mechanics*, Vol. 32, Jan. 2000, pp. 203–240. doi:10.1146/annurev.fluid.32.1.203

[14] Sreenivasan, K. R., "On Local Isotropy of Passive Scalars in Turbulent Shear Flows," *Proceedings: Mathematical and Physical Sciences*, Vol. 434, No. 1890, 1991, pp. 165–182. doi:10.1098/rspa.1991.0087

[15] Guezennec, Y., Stretch, D., and Kim, J., "The Structure of Turbulent Channel Flow with Passive Scalar Transport," *Proceedings of the Summer Program 1990*, Center for Turbulence Research, Stanford, Stanford Univ., Palo Alto, CA, 1990, pp. 127–138.

[16] Antonia, R. A., Abe, H., and Kawamura, H., "Analogy Between Velocity and Scalar Fields in a Turbulent Channel Flow," *Journal of Fluid Mechanics*, Vol. 628, June 2009, pp. 241–268. doi:10.1017/S0022112009006181

[17] Gordeyev, S., and Smith, A. E., "Studies of the Large-Scale Structure in Turbulent Boundary Layers Using Simultaneous Velocity-Wavefront Measurements," *AIAA Aviation*, AIAA Paper 2016-3804, 2016. doi:10.2514/6.2016-3804

[18] Vanderwel, C., and Tavoularis, S., "Scalar Dispersion by Coherent Structures in Uniformly Sheared Flow Generated in a Water Tunnel," *Journal of Turbulence*, Vol. 17, No. 7, 2016, pp. 633–650. doi:10.1080/14685248.2016.1155713

[19] Antonia, R. A., Danh, H. Q., and Prabhu, A., "Response of a Turbulent Boundary Layer to a Step Change in Surface Heat Flux," *Journal of Fluid Mechanics*, Vol. 80, April 1977, pp. 153–177. doi:10.1017/S002211207700158X

[20] Smith, A., Gordeyev, S., Saxton-Fox, T., and McKeon, B., "Subsonic Boundary-Layer Wavefront Spectra for a Range of Reynolds Numbers," *45th AIAA Plasmadynamics and Lasers Conference*, AIAA Paper 2014-2491, 2014. doi:10.2514/6.2014-2491

[21] Rought, R., "Identification of Thermally-Tagged Coherent Structures in the Zero Pressure Gradient Turbulent Boundary Layer," M.S. Thesis, California Inst. of Technology, Pasadena, CA, 2013.

[22] Raffel, M., Willert, C. E., Scarano, F., Kahler, C. J., Wereley, S. T., and Kompenhans, J., *Particle Image Velocimetry: A Practical Guide*, 3rd ed., Springer, New York, 2018. doi:10.1007/978-3-319-68852-7

[23] DeGraaff, D. B., and Eaton, J. K., "Reynolds-Number Scaling of the Flat-Plate Turbulent Boundary Layer," *Journal of Fluid Mechanics*, Vol. 422, Nov. 2000, pp. 319–346. doi:10.1017/S0022112000001713

[24] Malley, M., Sutton, G., and Kincheloe, N., "Beam-Jitter Measurements of Turbulent Aero-Optical Path Differences," *Applied Optics*, Vol. 31, No. 22, 1992, pp. 4440–4443. doi:10.1364/AO.31.004440

[25] Gladstone, J. H., and Dale, T. P., "Researches on the Refraction, Dispersion, and Sensitiveness of Liquids," *Philosophical Transactions of the Royal Society of London*, Vol. 153, Jan. 1863, pp. 317–343. doi:10.1098/rstl.1863.0014

[26] Buchdahl, H., *An Introduction to Hamiltonian Optics*, Vol. 18, Cambridge Univ. Press, New York, 1993.

[27] Brown, G. L., and Thomas, S. W., "Large Structure in a Turbulent Boundary Layer," *Physics of Fluids*, Vol. 20, No. S243, 1977, pp. S243–S252. doi:10.1063/1.861737

[28] McKeon, B. J., and Sharma, A. S., "A Critical-Layer Framework for Turbulent Pipe Flow," *Journal of Fluid Mechanics*, Vol. 658, Sept. 2010, pp. 336–382. doi:10.1017/S002211201000176X

[29] Sharma, A. S., and McKeon, B. J., "On Coherent Structure in Wall Turbulence," *Journal of Fluid Mechanics*, Vol. 728, Aug. 2013, pp. 196–238. doi:10.1017/jfm.2013.286

[30] McKeon, B. J., "The Engine Behind (Wall) Turbulence: Perspectives on Scale Interactions," *Journal of Fluid Mechanics*, Vol. 817, April 2017. doi:10.1017/jfm.2017.115

Downloaded by UNIVERSITY OF NOTRE DAME on July 5, 2019 | http://arc.aiaa.org | DOI: 10.2514/1.J058088

[31] Saxton-Fox, T., and McKeon, B., "Coherent Structures, Uniform Momentum Zones and the Streamwise Energy Spectrum in Wall-Bounded Turbulent Flows," *Journal of Fluid Mechanics*, Vol. 826, Sept. 2017. doi:10.1017/jfm.2017.493

[32] Zaman, K. B. M. Q., and Hussain, A. K. M. F., "Taylor Hypothesis and Large-Scale Coherent Structures," *Journal of Fluid Mechanics*, Vol. 112, Nov. 1981, pp. 379–396. doi:10.1017/S0022112081000463

[33] Mathis, R., Hutchins, N., and Marusic, I., "Large-Scale Amplitude Modulation of the Small-Scale Structures in Turbulent Boundary Layers," *Journal of Fluid Mechanics*, Vol. 628, June 2009, pp. 311–337. doi:10.1017/S0022112009006946

[34] Chung, D., and McKeon, B. J., "Large-Eddy Simulation of Large-Scale Structures in Long Channel Flow," *Journal of Fluid Mechanics*, Vol. 661, Oct. 2010, pp. 341–364. doi:10.1017/S0022112010002995

[35] Kovasznay, L. S. G., Kibens, V., and Blackwelder, R. F., "Large-Scale Motion in the Intermittent Region of a Turbulent Boundary Layer," *Journal of Fluid Mechanics*, Vol. 41, No. 2, 1970, pp. 283–325. doi:10.1017/S0022112070000629

[36] Eisma, J., Westerweel, J., Ooms, G., and Elsinga, G. E., "Interfaces and Internal Layers in a Turbulent Boundary Layer," *Physics of Fluids*, Vol. 27, No. 5, 2015, Paper 055103. doi:10.1063/1.4919909

[37] Klewicki, J. C., and Hirschi, C. R., "Flow Field Properties Local to Near-Wall Shear Layers in a Low {R}eynolds Number Turbulent Boundary Layer," *Physics of Fluids*, Vol. 16, No. 11, 2004, pp. 4163–4176. doi:10.1063/1.1801891

[38] Chen, C. H. P., and Blackwelder, R. F., "Large-Scale Motion in a Turbulent Boundary Layer: A Study Using Temperature Contamination," *Journal of Fluid Mechanics*, Vol. 89, No. 1, 1978, pp. 1–31. doi:10.1017/S0022112078002438

[39] Adrian, R. J., "Hairpin Vortex Organization in Wall Turbulence," *Physics of Fluids*, Vol. 19, No. 4, 2007, Paper 041301. doi:10.1063/1.2717527

[40] Saxton-Fox, T., "Coherent Structures, Their Interactions, and Their Effects on Passive Scalar Transport and Aero-Optic Distortion in a Turbulent Boundary Layer," Ph.D. Thesis, California Inst. of Technology, Pasadena, CA, 2018.

L. Ukeiley
Associate Editor

Downloaded by UNIVERSITY OF NOTRE DAME on July 5, 2019 | http://arc.aiaa.org | DOI: 10.2514/1.J058088